

# Investigating mechanical properties of polymethylmethacrylate/silver nanoparticle composites by molecular dynamics simulation

Shin-Pon Ju · Hsing-Yin Chen · Che-Wei Shih

Received: 25 May 2017 / Accepted: 15 December 2017 / Published online: 26 December 2017  
© Springer Science+Business Media B.V., part of Springer Nature 2017

**Abstract** The molecular dynamics simulation (MD) was carried out to investigate the mechanical properties of pristine polymethylmethacrylate (PMMA) and the composites of PMMA mixed with the silver nanoparticles (PMMA/AgNPs) at two AgNP weight fractions at 0.60 and 1.77 wt%. From the stress–strain profiles by the tensile process, it can be seen that the improvement on Young’s modulus is insignificant at these lower AgNP fractions. The tensile strength of pristine PMMA can be slightly improved by the embedded AgNPs at 1.77 wt%, because the local density and strength of PMMA in the vicinity of AgNP surface within about 8.2 Å are improved. For the temperature effect on the mechanical properties of pristine PMMA and PMMA/AgNP composite, the Young’s moduli and strength of pristine PMMA and PMMA/AgNP composite significantly decrease at temperatures of 450 and 550 K, which are close to the predicted melting temperature of pristine PMMA about 460 K. At these temperatures, the PMMA materials become more ductile and the AgNPs within the PMMA matrix display higher mobility than those at 300 K. When the tensile strain increases, the AgNPs tend to get closer and the fracture appears at the PMMA part, leading to the close values of Young’s modulus and

ultimate strength for pristine PMMA and PMMA/AgNP composite at 450 and 550 K.

**Keywords** Molecular dynamics · PMMA · Ag nanoparticle · Mechanical property · Modeling · Simulation

## Introduction

Developing polymer-based composites by adding different fillers has been demonstrated to be a promising method for modifying the material properties of polymers, and this fabrication process makes new composite materials possible for industrial applications (Agag et al. 2001; Rafiee et al. 2009). For examples, properties of pristine polymers such as mechanical strength (Ahmad et al. 2010), elasticity (Leszczyńska et al. 2007; Zhao et al. 2012), plasticity (Petersson et al. 2007; Zhi et al. 2009), electrical conductivity (Lu et al. 2003; Zhou et al. 2011), and thermal conductivity (Coleman et al. 2006; Kendall and Siviour 2014) can be significantly enhanced after the polymer matrixes are mixed with the well-dispersed fillers.

Polymethylmethacrylate (PMMA) is one of the most widely used thermoplastic polymers because of its excellent mechanical properties and physical properties. The density of PMMA is about 1.15–1.19 g/cm<sup>3</sup> (van Oss and Good 1989), which is about half of glasses (2.40–2.80 g/cm<sup>3</sup>), but PMMA has the impact strength about 40–60 GPa, which is 10 times higher than the

---

S.-P. Ju · C.-W. Shih  
Department of Mechanical and Electro-Mechanical Engineering,  
National Sun Yat-Sen University, Kaohsiung 804, Taiwan

S.-P. Ju (✉) · H.-Y. Chen  
Department of Medicinal and Applied Chemistry, Kaohsiung  
Medical University, Kaohsiung 807, Taiwan  
e-mail: jushin-pon@mail.nsysu.edu.tw

ordinary glasses (Heijboer 1967). PMMA's thermal stability with heat resistance is around 65 to 100 °C (Gilman 1999), and its melting point is typically 135 to 160 °C (Nishi and Wang 1975). Because of these excellent mechanical properties and thermal stability, PMMA is usually applied to bullet-proof glass and the military aircraft windshield. Many potential fillers such as graphite (Zheng and Wong 2003), carbon fiber (Zeng et al. 2004), and epoxy (Park and Jana 2003) have been mixed with the pristine PMMA for further enhancing its mechanical properties. These composites have been extensively used in different fields such as automotive industry (window, screens) and biomedical applications (wound dressing) (Jia et al. 1999).

Many experimental approaches have been conducted to investigate the properties of PMMA composites. For examples, Banks-Sills studied the mechanical properties of PMMA blended with functionalized carbon nanotubes at different weight percentages by the grafting from (GF) and the grafting to (GT) methods (Banks-Sills et al. 2016). They indicated that the elastic modulus of PMMA/carboxylated CNT composites significantly increases when the addition of CNTs is higher than 3 wt%. Moreover, the PMMA matrix with the low CNT content of functionalized and non-functionalized CNTs possesses the lower elastic modulus than that of neat PMMA. Blivi studied the mechanical properties and thermal stability of PMMA blended with the silica nanoparticles of different sizes (Blivi et al. 2016). Their experimental results show that all nanocomposites have the Young's moduli higher than that of pure PMMA. The Young's modulus and the glass transition temperature of nanocomposites become higher when the smaller silica nanoparticle is used. Wang reported that PMMA displays 20% increase in the tensile strength and 50% increase in the tensile modulus after PMMA is mixed with the fully exfoliated layered silicate clay at 3 wt% (Wang et al. 2002). At the low SWNT concentration of 0.114 wt%, Skákalová stated that the tensile strength of PMMA can be improved 30 times higher than that of pristine PMMA (Skakalova et al. 2005). Fan investigated the mechanical properties of PMMA mixed with functionalized graphene, and their results showed that the tensile strength and Young's modulus can be enhanced from 9.8 to 63.2 GPa and from 1 to 3.42 GPa when the functionalized graphene with 0.7 wt% was blended with PMMA (Fan et al. 2012). Guo studied the mechanical properties of PMMA blended with the aluminum nanoparticles of 3 vol%; they found that the

ultimate stress and Young's modulus can be enhanced up to 65 and 85% higher than those of pure PMMA (Guo et al. 2006).

It is well known that the Ag nanoparticle (AgNP) is superior to other nanostructured metal particles for many reasons, such as its unique mechanical, optical, electrical, and chemical properties (Kim et al. 2007; Lee et al. 2003; Quang Huy et al. 2013) as well as its strong inhibiting and antimicrobial effects (Morsy and Al-Daous 2013; Mulfinger et al. 2007). Therefore, it seems likely that a PMMA matrix could demonstrate improved mechanical properties with the addition of Ag nanoparticle filler (Lee et al. 2006). For example, Sodagar studied the mechanical properties of PMMA/AgNP composites with the Ag percentage of 0.05 and 0.2 wt%. The results indicate that the flexural strength is only improved slightly and there are almost no differences between these two composites in this blending ratio (Sodagar et al. 2012). In Hamed-Rad's study, it can be seen that the compressive strength can be enhanced from 102.16 to 121.19 MPa when PMMA mixed with silver nanoparticles about 5 wt% (Hamed-Rad et al. 2014).

The experimental studies mentioned above have reported that PMMA/AgNP composites can enhance the mechanical properties of pristine PMMA. However, the PMMA and AgNP interaction mechanism causing this enhancement in mechanical properties is very difficult to obtain by the experimental approach. Consequently, computer simulation approaches have been used as alternative methods to illustrate the interaction mechanism between PMMA and AgNP at the atomic scale. Molecular dynamics (MD) simulation is a powerful simulation method to investigate the interaction between atoms on the basis of accurate interaction potential. By using the MD simulation, Lin studied the mechanical properties of graphene/PMMA nanocomposites at different temperatures (Zhu et al. 2007). They indicated that the Young's modulus increases with the increasing graphene volume fraction and the PMMA with graphene of 11% displays the highest Young's modulus. However, the Young's moduli of all nanocomposites decrease when the temperature rises from 300 to 500 K. Nayebi studied the mechanical properties of graphene-polythiophene (PT) nanocomposite by molecular dynamics simulation at different temperatures (Nayebi and Zaminpayma 2016). They showed that the Young's modulus and breaking strain increase with the increasing graphene weight concentration. The breaking strain,

breaking stress, and Young's moduli decrease when the temperature rises from 100 to 700 K due to decrease of interaction energy. Yang has investigated the influence of the Thrower–Stone–Wales (TSW) defect on the physical behavior of CNT/polypropylene (PP) composites. The Young's modulus and the transverse and longitudinal shear moduli of the composites increase due to the stronger interfacial adhesion between the defected CNTs and the PP matrix (Yang et al. 2013). Adnan investigated the effect of buckyball size on the elastic properties of PE/buckyball composites. Their results demonstrated that elastic properties of PE/buckyball can be significantly improved with the reduction of buckyball size (Adnan et al. 2007). Zhu studied the mechanical properties of epoxy Epon 862 matrix with single-walled carbon nanotubes (CNTs) for three systems—a long CNT-reinforced Epon 862 composite, a short CNT-reinforced Epon 862 composite, and the Epon 862 matrix itself. The simulation results show that the long CNT-reinforced Epon 862 composite is at least 10 times stiffer than the pure Epon 862 matrix. Even for the short CNT-reinforced Epon 862 composite, its effective Young's modulus also increases by roughly 20% as compared to the Epon 862 matrix (Zhu et al. 2007).

However, to the best of our knowledge, none of the large system of polymethylmethacrylate/silver (PMMA/Ag) nanoparticle composite has been explored for assessing their physicochemical properties using simulation technique. In this study, we employed the MD simulation to model the PMMA/AgNP composites and compared its mechanical properties to that of pristine PMMA. The Young's modulus, mechanical strength, and fracture mechanism of all PMMA–AgNP systems were obtained by the corresponding stress–strain profiles. These results could be further applied to relevant polymer/nanoparticle systems.

## Simulation methods

For exploring the mechanical properties of pristine PMMA and PMMA/AgNP composites, molecular dynamics simulations were carried out by using LAMMPS (Cheng and Grest 2013). Figure 1a–e shows the skematic diagrams of one AgNP, a PMMA chain, pristine PMMA model, PMMA/AgNP composite with one AgNP, and PMMA/AgNP composite with two AgNPs, respectively. By the following equation (Stepanov et al. 2002), the AgNPs with the diameter ranging from 2 to

20 nm were blended with the PMMA matrix. Because of the computational limitation on the atom number for MD simulation, the AgNP with the 2 nm in diameter was used, which was directly cut from the Ag F.C.C. crystal structure. For the F.C.C. metal nanoparticles, the (111) and (100) planes are two common facets on the NP surfaces when the NP diameters are larger than 2 nm. In Fig. 1a, the AgNP with the (111) and (100) facets can be seen, so the current AgNP can reflect the structural property of AgNP used in the related experiment.

The PCFF (polymer consistent force field) force field (Sun 1994) is used to describe the interactions between PMMA atoms, because PCFF has been parameterized and validated for PMMA with the valence terms for bond stretching, angle bending, dihedral, and improper interactions as well as the coupling between them. The non-bonded terms include the electrostatic and Van der Waals interactions, and the latter is represented by the Lennard–Jones (LJ) 9-6 potential. The long-range electrostatic interactions were evaluated using the PPPM (particle–particle–particle–mesh) summation in the current study.

The many-body tight-binding potential is used to model the interaction between Ag atoms of AgNP. This model sums the band energy, which is characterized by the second moment of the d-band density of state, and a pairwise potential energy of the Born–Mayer type, i.e.,

$$E_i = - \left\{ \sum_j \xi^2 \exp \left[ -2q \left( \frac{r_{ij}}{r_0} - 1 \right) \right] \right\}^{1/2} + \sum_j A \exp \left[ -p \left( \frac{r_{ij}}{r_0} - 1 \right) \right] \quad (1)$$

where  $\xi$  is the effective hopping integral,  $r_{ij}$  is the distance between atoms  $i$  and  $j$ , and  $r_0$  is the first neighbor distance. The parameters of tight-binding potential for Ag are listed in Table 1 (Karolewski 2001).

For accurately modeling the interaction between the AgNP and PMMA, the optimized PCFF force field developed by Heinz was used (Heinz et al. 2008). The optimized PCFF force field can precisely simulate metal and hybrid interfaces with organic, inorganic, and biological compounds and can also effectively improve clarity about the various roles in the mixed (metallic and non-metallic elements)

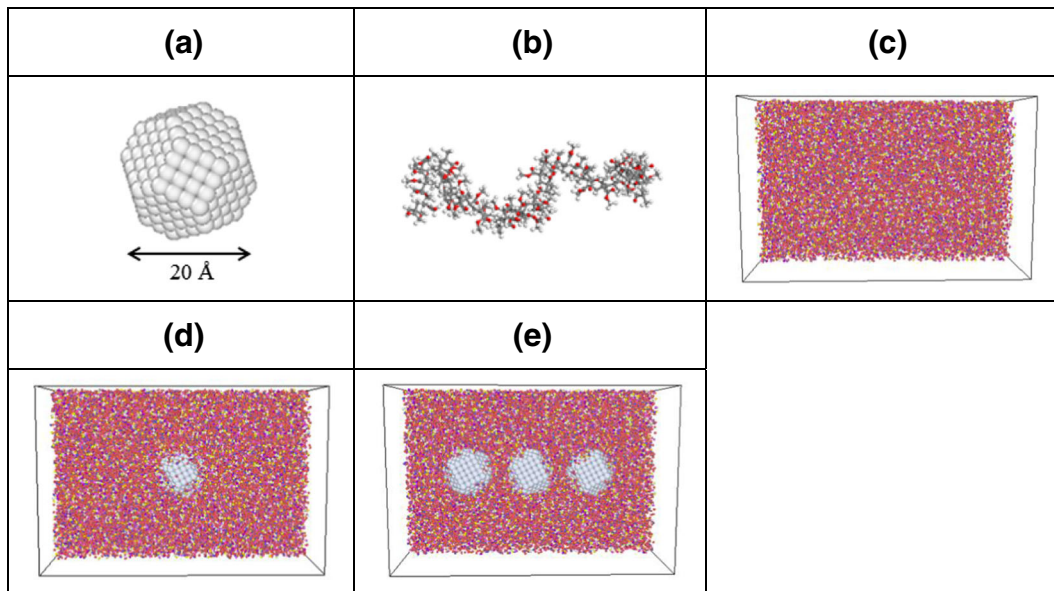


**Fig. 1** Schematic diagrams of **a** Ag nanoparticle, **b** one PMMA chain, **c** PMMA model, **d** PMMA/AgNP (0.60%) model, and **e** PMMA/AgNP (1.77%)

system. The Lennard–Jones 9-6 potential is given by the following equation:

$$E = \varepsilon \left[ 2 \left( \frac{\sigma}{r} \right)^9 - 3 \left( \frac{\sigma}{r} \right)^6 \right] r < r_c \quad (2)$$

where  $\varepsilon$  is the depth of the potential well,  $\sigma$  is the finite distance at which the inter-particle potential is zero,  $r$  is the distance between the interaction particles,  $r_c$  is the cutoff distance. The optimized PCFF force field parameters of Ag are shown in Table 2 (Heinz et al. 2008). It should be noted that these Ag parameters were used to determine the interaction parameters between Ag atom and PMMA atoms of different types by the sixth power mixing rule as the following equation:

$$\varepsilon_{ij} = \frac{2\sqrt{\varepsilon_i \varepsilon_j} \times \sigma_i^3 \sigma_j^3}{\sigma_i^6 + \sigma_j^6} \quad \sigma_{ij} = \left( \frac{\sigma_i^6 + \sigma_j^6}{2} \right)^{\frac{1}{6}} \quad (3)$$

**Table 1** The tight-binding potential parameters of Ag

	$A$ (eV)	$\xi$ (eV)	$p$	$Q$	$r_0$ (Å)
Ag	0.103	1.178	10.928	3.139	2.89

For the pristine PMMA system, a PMMA chain with 50 monomers was used and a total of 132 PMMA chains were adopted to construct the simulation system. The procedure to obtain the equilibrium configuration is described as follows: (1) the conjugate gradient method was used to optimize the structure, and energy convergence condition was set to  $10^{-6}$  kcal/mol, with maximum iterations of  $10^5$ . (2) After optimization, the system was brought to equilibrium at 1000 K for 200 ps at 1 atm. (3) The system was then quenched from 1000 to 300 K with a cooling rate of 3.5 K/ps at 1 atm by an isobaric–isothermal ensemble (NPT). (4) Finally, the MD simulation at 300 K and 1 atm was performed for an additional 200 ps by the NPT ensemble to reach the equilibrium condition. The density of pristine PMMA system through the simulated annealing process is about  $1.12 \text{ g/cm}^3$ , which is slightly lower than that of the corresponding experimental value about  $1.15\text{--}1.19 \text{ g/cm}^3$  (van Oss and Good 1989) by 3% within the acceptable range.

For PMMA/AgNP composites, an AgNP with the diameter about 20 Å, which consists of 405 Ag atoms,

**Table 2** The parameters of optimized PCFF force field for Ag

	$\varepsilon$ (kcal/mol)	$\sigma$ (Å)
Ag	3.73	3.005

was used. For investigating the Ag atom fraction effect on the PMMA/AgNP mechanical properties, the PMMA matrixes with one and three AgNPs were considered and the corresponding weight fractions of these two PMMA/AgNP composites were about 0.60 and 1.77%, respectively. These different weight fraction composites are hereafter referred to as AgNP (0.60%) and AgNP (1.77%) for describing our simulation results. For inserting the AgNP into the PMMA matrix, an empty spherical space with the radius of 12 Å was created within the interior region of PMMA matrix by the extrusion of a virtual repulsive spherical surface with the radius starting from 0.1 to 12 Å. The increment of increasing the radius of virtual repulsive spherical surface is about 0.01 Å, and the geometrical optimization was carried out before applying the next increment. After the AgNP was placed into the virtual spherical region, the system was annealed from 1000 to 300 K with a cooling rate of 3.5 K/ps for relaxing the PMMA/AgNP interfacial geometry by the NPT ensemble at 1 atm. The Nosé–Hoover thermostat and barostat (Hoover 1985) were used in all MD cases, and the detailed information of system size at strain of 0, PMMA chain number, Ag atom number, and the total atom number about three simulation models can be seen in Table 3.

For the tensile simulation, the strain was applied to *x* dimension and the increment is 0.25% and the periodic boundary conditions were applied in all directions. After each tensile increment, the MD simulation in the NVT ensemble that was used for 5 ps was used to relax the system. Then, the stress was recorded every 0.1 ps in order to obtain the average stresses for another 5 ps before imposing the next tensile increment. The tensile stresses at different strains were determined by the following equation (Ju et al. 2014):

$$\sigma_{mn} = \frac{1}{V_s} \sum_i \left[ m_i V_i^m V_i^n - \frac{1}{2} \sum_j \frac{\partial \theta(r_{ij})}{\partial r_{ij}} \frac{r_{ij}^m r_{ij}^n}{r_{ij}} \right] \quad (4)$$

where *m<sub>i</sub>* is the mass of atom *i*, *V<sub>s</sub>* is the system volume, and *V<sub>i</sub><sup>m</sup>* and *V<sub>i</sub><sup>n</sup>* are the velocities of atom *i* along the m-

and n- dimensions,  $\theta(r_{ij})$  is the potential function, and  $r_{ij}^m$  and  $r_{ij}^n$  are two components of the vector from atoms *i* to *j* along the m- and n- dimensions.

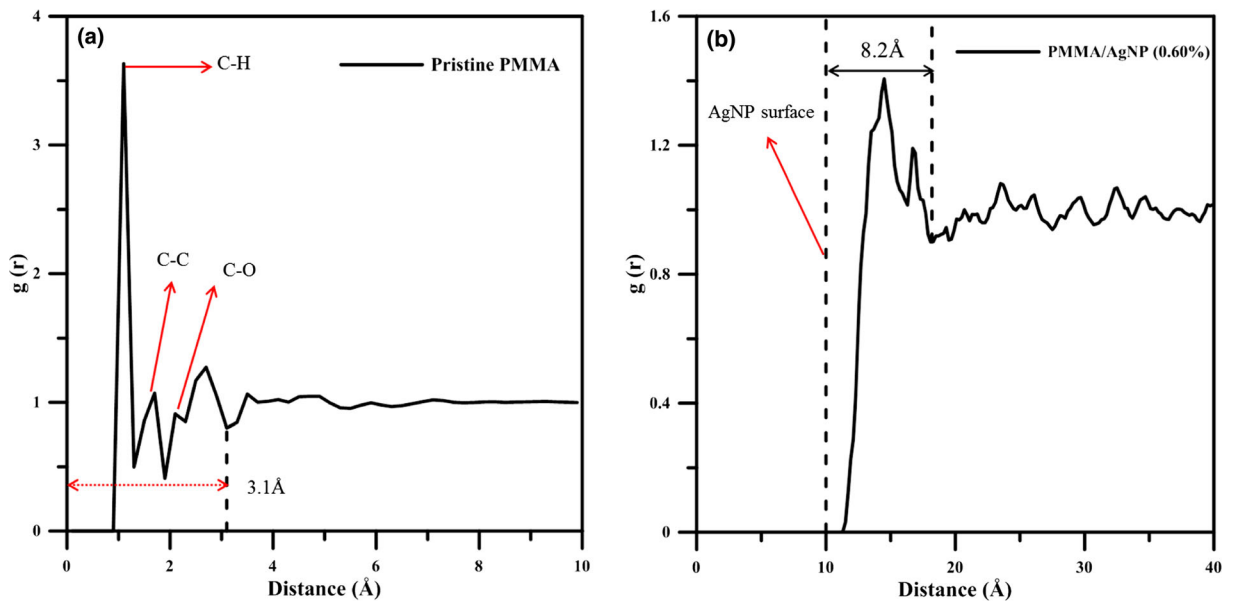
### Results and discussion

Figure 2a, b shows the radial distribution functions (RDFs) of all pristine PMMA atom pair types and PMMA/AgNP pair types in the PMMA/AgNP systems, respectively. It should be noted that the RDF origin of the PMMA/AgNP system is located at the mass center of AgNP. In Fig. 2a, the RDF profile shows three distinct narrow peaks at 1.1, 1.7, and 2.2 Å for the bonded C–H, C–C, and C–O pairs. The broader peak ranging from 1.7 to 3.1 Å represents the first peak of the non-bonding RDF profile, indicating that the influence distance of the non-bonding interaction around one atom is about 3.1 Å for the pristine PMMA. For the PMMA/AgNP composite, the prominent first two peaks at 14.7 and 18.2 Å can be seen in Fig. 2b, and their thickness from the AgNP surface is about 8.2 Å, indicating that atoms of PMMA chains within 8.2 Å in the vicinity of AgNP surface still have strong interaction strength with AgNP and possess higher local density.

Figure 3 shows the stress–strain curves of the pristine PMMA and PMMA/AgNP composites at AgNP (0.60%) (one AgNP) and AgNP (1.77%) (three AgNPs) of Ag atoms under tensile loading at 300 K. For these three stress–strain curves, it can be seen that, from 0 to about 0.05, the stress is linearly proportional to the strain, then increases parabolically with the increasing strain up to the point of ultimate stress. One can see the ultimate stresses roughly fluctuate at a constant value within certain strain ranges for these three cases. After the strain exceeds the strain range corresponding to the ultimate stress, the stress gradually decreases for these three cases. It can be seen that the ultimate stresses of two PMMA/AgNP composites are very similar to that of pristine PMMA. The Young’s modulus was obtained from the slope of linearly fitted line

**Table 3** The detailed information about pristine PMMA, PMMA/AgNP (0.60%), and PMMA/AgNP (1.77%)

	Box dimensions (Å <sup>3</sup> )	Number of PMMA chains	Number of Ag atoms	Total atom numbers
PMMA	131.4 × 86.1 × 86.2	132	0	99,264
PMMA/AgNP (0.60%)	131.9 × 86.8 × 85.4	132	405	99,669
PMMA/AgNP (1.77%)	134.8 × 86.6 × 86.3	132	1215	100,479



**Fig. 2** Radial distribution functions (RDFs) for **a** pristine PMMA and **b** PE/AgNP (0.60%). It should be noted that the origin of PMMA/AgNP (0.60%) RDF is the mass center of AgNP

with the data at strains smaller than 0.02. In Fig. 3, however, one can see that all the curves in the elastic region are perfectly superimposed and the tensile stress does not seem to increase with the Ag weight fraction. For getting better linearly fitted slopes of stress–strain curves, several

lower tensile strain increments (0.1, 0.05, and 0.01%) were used to prepare more fitting data within the elastic region for the least-square method. The Young's moduli derived from the fitted slopes display no relationship with the AgNP fractions at 0.60 and 1.77%, and their

**Fig. 3** Stress–strain curves of pristine PMMA, PMMA/AgNP (0.60%), and PMMA/AgNP (1.77%)

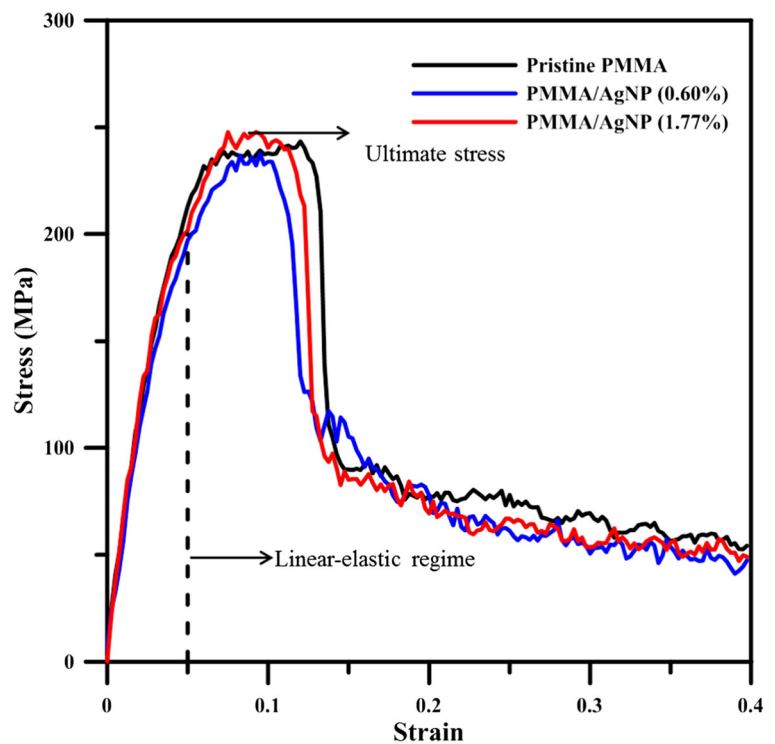


**Table 4** The Young’s modulus and ultimate stress of pristine PMMA at different Ag weight fractions

AgNP weight fraction (%)	0	0.60	1.77
Ultimate stress (MPa)	242.43	237.69	247.82

average values are close to 5.6 GPa. For ultimate stress or tensile strength, it can be seen from Table 4 that the tensile strength can be slightly enhanced from 242.43 to 247.82 MPa for PMMA/AgNP (1.77%).

To investigate the local structural rearrangement, the atomic local shear strain  $\eta_i^{Mises}$  of an individual atom, introduced by Shimizu et al. (2007), was used to monitor the development of shear transition zones (STZ). The detailed definition of  $\eta_i^{Mises}$  can be found in reference (Wang et al. 2010) and is therefore not introduced here. A large  $\eta_i^{Mises}$  value indicates that atom *i* is under local plastic and shear deformation, whereas a small  $\eta_i^{Mises}$  value implies that atom *i* undergoes a small amount of movement relative to all its first neighbor atoms or atom *i* is under local elastic deformation. The

distributions of atomic local shear strain were calculated and shown by OVITO (Stukowski 2009), and the structures at strain of 0 for all three cases are the references for calculating the atomic local shear strains at different tensile strains.

Figure 4a–h shows the snapshots of pristine PMMA with atomic  $\eta_i^{Mises}$  values at strains of 0.02, 0.08, 0.1, 0.12 (ultimate stress), 0.1225 (ultimate stress), 0.125 (abrupt drop begins), 0.1475 (abrupt drop ends), and 0.3. Three snapshots within the strain range (0.12, 0.1225, 0.125) with the constant ultimate stress are used to investigate the development of local structural deformation. In the  $\eta_i^{Mises}$  distribution at strain of 0.02, which is the upper bound of strain for calculating the Young’s modulus, Fig. 4a demonstrates that the  $\eta_i^{Mises}$  values of most atoms are close to 0, indicating that local elastic deformation is dominant at this strain. As the strain continuously increases from 0.02 to 0.1, some local regions with atoms having larger  $\eta_i^{Mises}$  values distribute randomly within the pristine PMMA as shown in Fig. 4b, c. At the strains of 0.12 and 0.1225 shown in

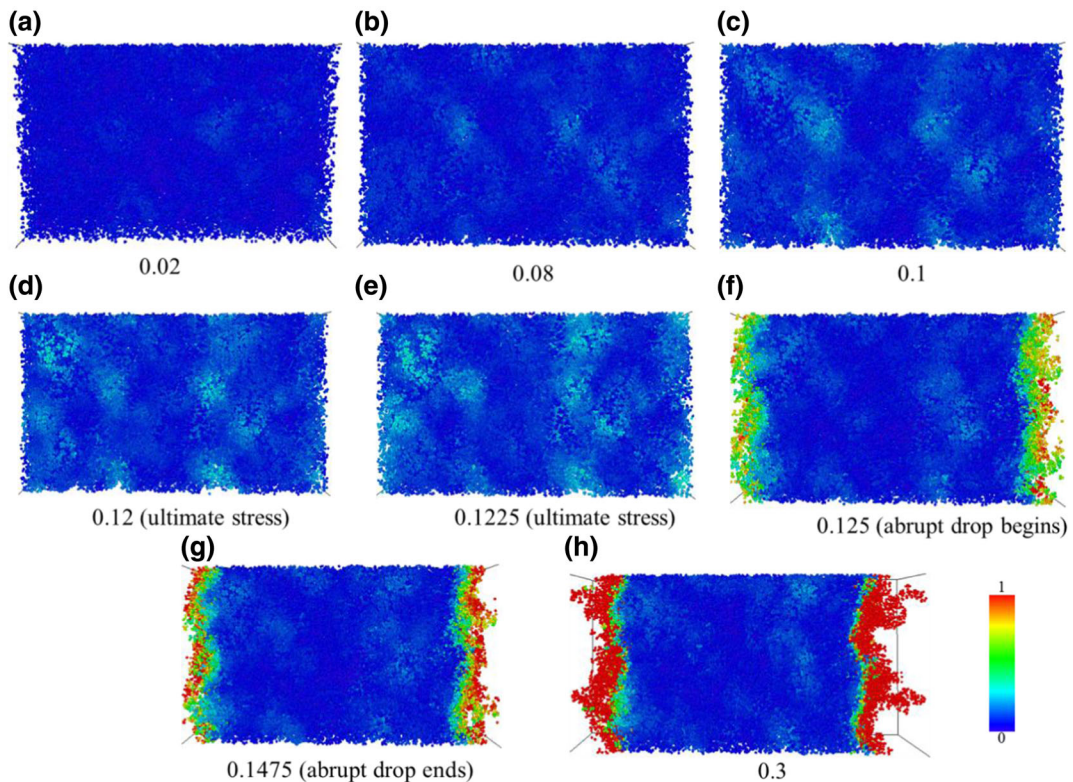


**Fig. 4** Uniaxial tensile deformation snapshots of pristine PMMA at **a** strain of 0.02, **b** 0.08, **c** 0.1, **d** 0.12 (ultimate stress), **e** 0.1225 (ultimate stress), **f** 0.125 (abrupt drop begins), **g** 0.1475 (abrupt

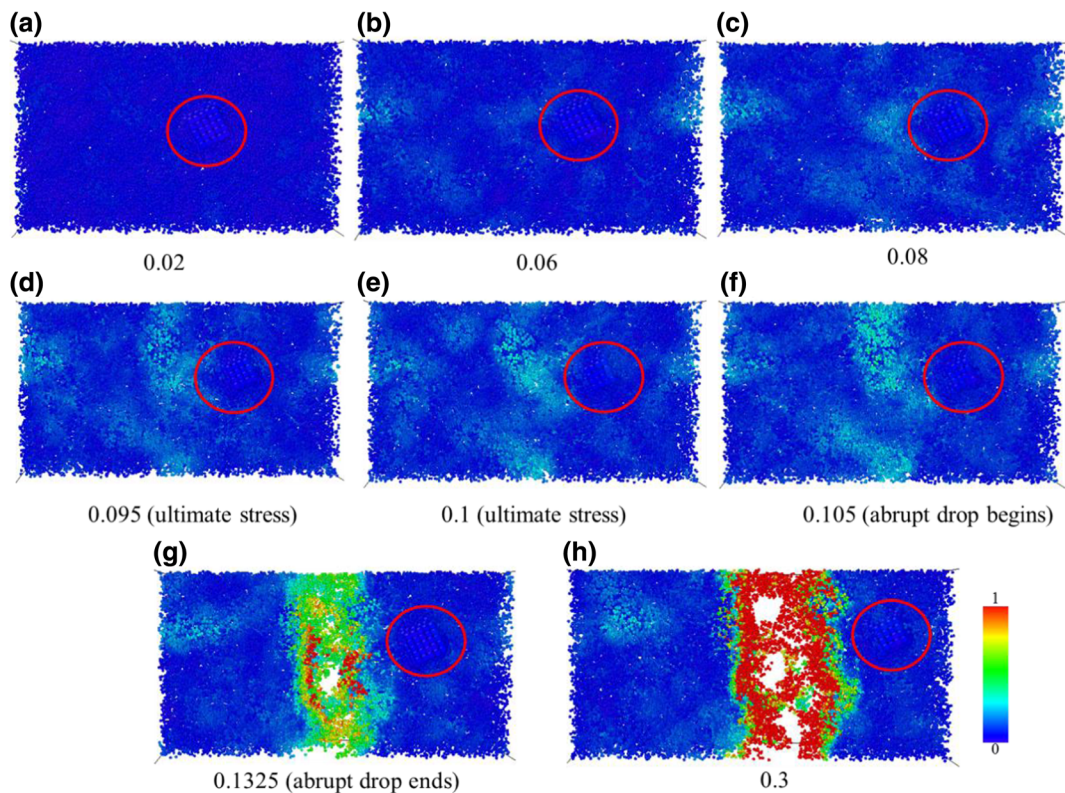
drop ends), and **h** strain of 0.3. The atoms are colored by their corresponding local shear strain values according to the referenced structure at strain of 0

Fig. 4d, e, the local deformation distributions in Fig. 4c gradually become wider. As the strain reaches the value, at which the stress just begins the abrupt drop from the ultimate stress, voids within the PMMA appear and the atoms around these voids undergo serious local shear deformation as shown in Fig. 4f. It can be seen that the local deformed structures with higher  $\eta_i^{\text{Mises}}$  values as shown in Fig. 4e have been relaxed when the voids appear. When the strain becomes further larger, the voids at strain of 0.125 have continuously grown, leading to the fracture of PMMA, as shown in Fig. 4g, h.

The snapshots for PMMA/AgNP (0.60%) and PMMA/AgNP (1.77%) during the tension process are shown in Figs. 5 and 6, respectively. The Ag nanoparticles within the PMMA matrixes are indicated by the red circles. For PMMA/AgNP (0.60%), as the strain increases from 0.02 to 0.08, the distributions of  $\eta_i^{\text{Mises}}$  values in the vicinity to the AgNPs become more significant as shown in Fig. 5c. This indicates that the PMMA atoms in this region are easily to undergo local shear deformation because of the interface formed by two materials with significantly different elasticity. The

same situation can be seen in Fig. 6c for PMMA/AgNP (1.77%) at strain of 0.08. At strains with the ultimate stresses as shown in Figs. 5–f and 6d–f, the distributions of  $\eta_i^{\text{Mises}}$  values in the vicinity to the AgNPs become larger. Although the local shear deformation of PMMA for these two PMMA/AgNP composites are more significant near AgNPs, the fracture of PMMA is not located at the region around AgNPs as shown in Figs. 5d and 6g. In Fig. 2b, one can see that the interaction between the AgNP and PMMA in the vicinity of AgNP surface leads to higher PMMA density around AgNPs, which also enhances the local strength of PMMA around AgNPs. Because the influence distance of the AgNP surface on the PMMA density is about 8.2 Å according to the RDF result, the voids are distributed at regions over 8.2 Å away from the AgNP surfaces. These voids grow continuously when the strain becomes larger, as shown in Figs. 5h and 6h.

To study the variation in porosity of each system during the tensile process, the porosity of system is calculated according to the following equation (Stukowski 2014):



**Fig. 5** Uniaxial tensile deformation snapshots of PMMA/AgNP (0.60%) at **a** strain of 0.02, **b** 0.06, **c** 0.08, **d** 0.095 (ultimate stress), **e** 0.1 (ultimate stress), **f** 0.105 (abrupt drop begins), **g** 0.1325

(abrupt drop ends), and **h** strain of 0.3. The atoms are colored by their corresponding local shear strain values according to the referenced structure at strain of 0



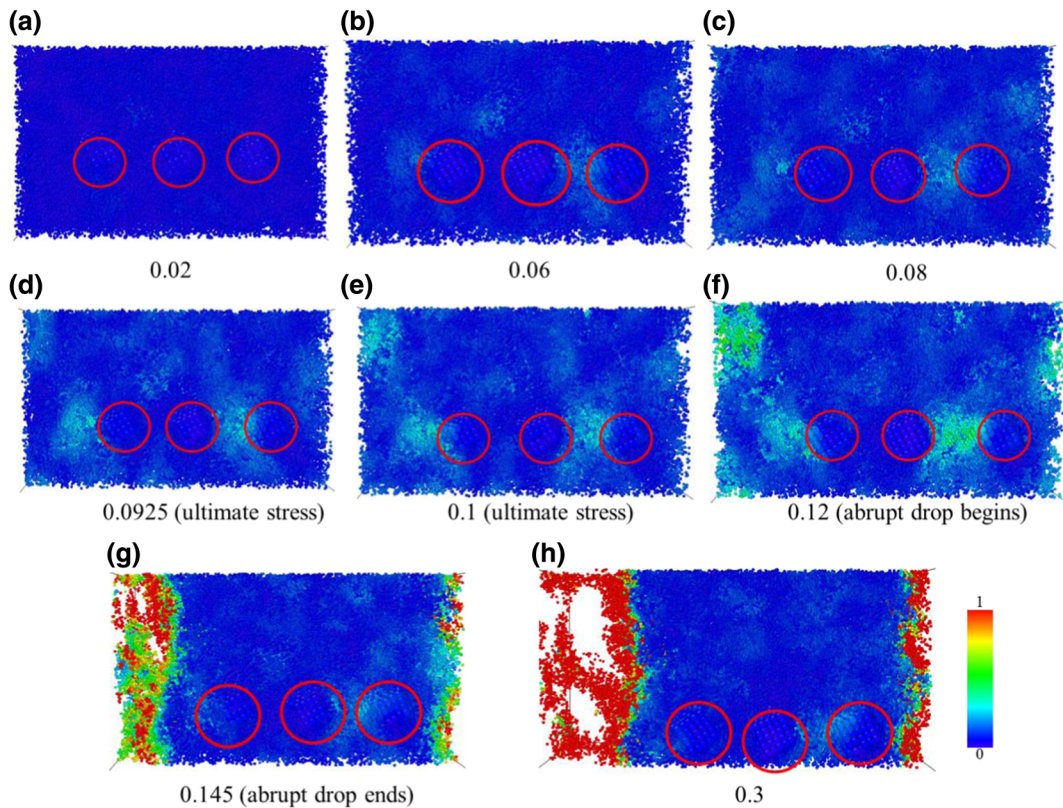


**Fig. 6** Uniaxial tensile deformation snapshots of PMMA/AgNP (1.77%) at **a** strain of 0.02, **b** 0.06, **c** 0.08, **d** 0.0925 (ultimate stress), **e** 0.1 (ultimate stress), **f** 0.12 (abrupt drop begins), **g** 0.145

(abrupt drop ends), and **h** strain of 0.3. The atoms are colored by their corresponding local shear strain values according to the referenced structure at strain of 0

$$Porosity = \frac{total\ volume - solid\ volume}{total\ volume} \% \quad (5)$$

where total volume is the volume of simulation system and the solid volume occupied by all atoms, as determined by the OVITO with a probe size of 5 Å. Figure 7 displays the porosity percentages of all cases at different strains. The porosity percentages at strains smaller than 0.04 are close to zero, indicating that the local damage is insignificant at this strain range. When strain increases from 0.04 to those of ultimate stresses, the porosity percentages slightly increase with the increasing tensile strain. When strains are larger than those of ultimate stresses, the porosity percentages significantly increase with increasing strain. At this strain range, it is obvious that, at the same strain, the porosity of pristine PMMA is higher than those of PMMA/AgNP (0.60%) and PMMA/AgNP (1.77%), with the porosity percentage lower at the higher Ag wt%. Comparing the fracture mechanism shown in Figs. 4, 5, and 6, one can see that the sizes of voids within the PMMA matrix are

relatively smaller at higher Ag wt%, because the interaction between the PMMA and AgNP enhances the local strength of PMMA. Consequently, the porosity at the lower Ag wt% is relatively higher, resulting in a lower PMMA strength.

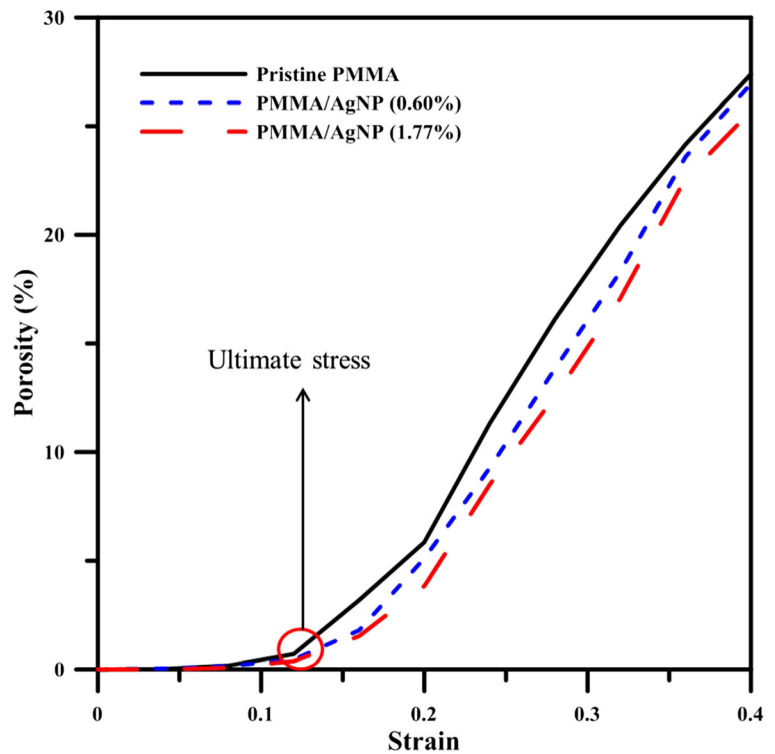
The increase of free volume was used to investigate the excess local volume increase during the tensile process. The definition of free volume increase percentage (FVIP) is

$$FVIP(\epsilon) = \frac{\sum_{i=1}^N V_i(\epsilon) - \sum_{i=1}^N V_i(0)}{\sum_{i=1}^N V_i(0)} \quad (6)$$

where  $V_i(\epsilon)$  is the volume of atom  $i$  at strain of  $\epsilon$ , and  $V_i(0)$  is the initial volume of the system at strain of 0. To obtain the atom volume created by the reference atom with its first neighbor atoms, the following equation, derived by Srolovitz, was used (Srolovitz et al. 1981):

$$V_i = \frac{4\pi}{3} a_i^3, \quad a_i = \frac{\sum_{ij}^{-1} r_{ij}^{-1}}{2\sum_{ij}^{-2} r_{ij}^{-2}} \quad (7)$$

**Fig. 7** Porosity percentage profiles of pristine PMMA, PMMA/AgNP (0.60%), and PMMA/AgNP (1.77%) at different strains



where  $a_i$  is the average radius of atom  $i$  and  $r_{ij}$  is the distance between atom  $i$  and its neighbor atom  $j$ . It should be noted that the first non-bonded neighbor atoms of a referenced atom at strain of 0 were used for calculating the atom volume during the tensile process.

Figure 8 shows the FVIP profiles at different strains for the pristine PMMA, as well as PMMA/AgNP (0.60%) and PMMA/AgNP (1.77%). In all profiles, the FVIP displays a distinct linear jump from 0 to 4% when the strain increases from 0 to 0.0025. It can be seen from Figs. 4a, 5a, and 6a that most atoms possess small local shear strain values, indicating that the volumes of most atoms conduct elastic expansion at this strain range. As the strain continuously increases from 0.02, the FVIP increases with increasing strain for all cases. At strains lower than that of ultimate strain, one can see that the FVIP profiles of these three cases closely match each other. When the strain is higher than that at ultimate stress, the FVIP of pristine PMMA increases more significantly than those of two PMMA/AgNP composites, indicating that the void sizes within the pristine PMMA grow more pronounced with increasing strain, as can be seen in Figs. 4h, 5h, and 6h. The FVIP of PMMA/AgNP (1.77%) is the lowest among three cases at all strains because the interaction between the AgNPs and PMMA

chains improves the strength of the PMMA matrix considerably more than that of PMMA/AgNP (0.60%).

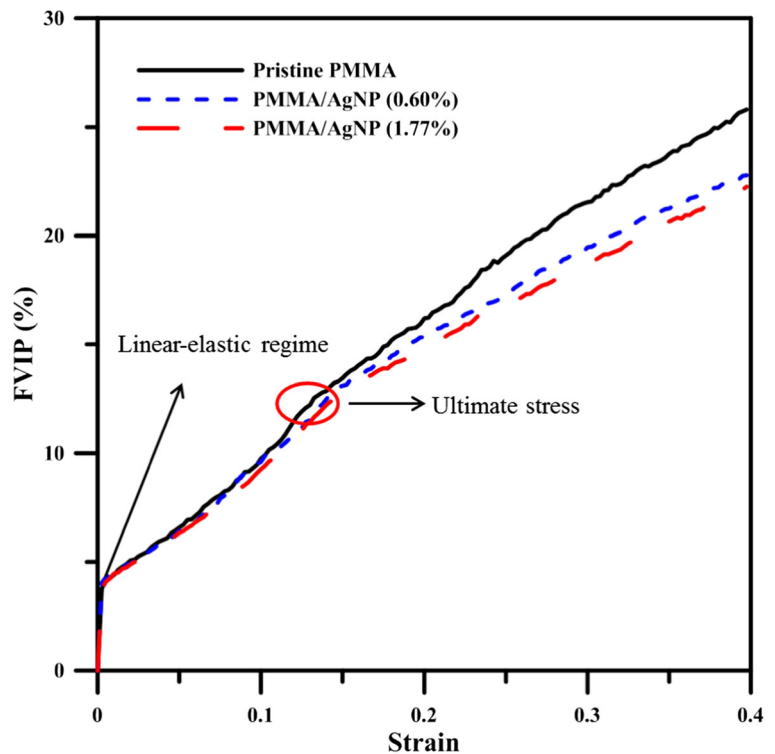
For exploring the local structural variations around different atom types, the variation in average distance of all non-bonded first neighbor atoms around a reference atom was determined for different atom types. The definition of the first neighbor distance variation of atom  $i$  is

$$R_i(\varepsilon) = \frac{\sum_j r_{ij}(\varepsilon) - \sum_j r_{ij}(0)}{\sum_j r_{ij}(0)} \quad (8)$$

where  $\sum_j r_{ij}(\varepsilon)$  is the sum of the distances between the referenced atom  $i$  and all its nonbonded first neighbor atom  $j$  at strain of  $\varepsilon$ , and  $\sum_j r_{ij}(0)$  is the sum of the distances at strain of 0.

For demonstrating our calculation results clearly, the symbols H, C2–C8, and O5, O6 are designated as the averaged distances of hydrogen atoms, carbon atoms, and oxygen atoms in PMMA. C2-type carbon atoms represent the methyl group of PMMA, and C3, C7, and C8 represent the backbone carbon atoms of PMMA, respectively. For the AgNP, the average distances for the surface Ag atoms and interior Ag atoms that do not contact PMMA atoms were also calculated. It should be

**Fig. 8** Free volume increase percentage profiles of pristine PMMA, PMMA/AgNP (0.60%), and PMMA/AgNP (1.77%) at different strains



noted that only the first non-bonded neighbor atoms around a referenced atom at strain of 0 were used for calculating the average distance during the tensile process. In Fig. 9, the profiles of average first neighbor distance variations are shown for the pristine PMMA, PMMA/AgNP (0.60%), and PMMA/AgNP (1.77%). An abrupt increase in the average first neighbor distances of all types can be seen from strain of 0 to 0.02 because of the elastic expansion under tensile loading. One can see from Fig. 9a–c that the C2 profiles display relatively sharp increases when the strains exceed those of the ultimate stresses in all cases, implying that breakage of the PMMA matrix by the tensile loading is initiated at the regions around the methyl group of PMMA chains. For the AgNP, the average first neighbor distance variation increases from 0 to about 0.01 at strain of 0.02 and then fluctuates at a constant of about 0.01. For the surface Ag atoms, the profiles of average first neighbor distance variation are most pronounced at strain of 0.02, as shown in Fig. 9b, c, indicating that the local atomic volume expansions of surface Ag atoms are more significant at the elastic region. As the strain increases from 0.02, the profiles display a turning point on ultimate stress; then, the curve of average first neighbor distance is shaken around after the strain over this turning point. This

phenomenon shows that the movement of surface Ag atoms is more significant. For the average first neighbor distance of the interior Ag atoms, the values almost keep constant (not exceed 1%) after the elastic range, indicating that the interior Ag atoms of AgNP are not influenced during the tensile process.

The temperature effect on mechanical properties of PMMA and PMMA/AgNP composites was also investigated by the molecular dynamics simulation. Only the simulation results of pristine and PMMA/AgNP (1.77%) were discussed. The NPT ensemble for 100 ps was applied to the temperature elevation process from 100 to 800 K at pressure of 1 atm. To obtain the melting temperatures ( $T_m$ ) of pristine PMMA and PMMA/AgNP (1.77%), the system volumes at different temperatures were sampled from 100 to 800 K at a temperature increment of 25 K.

Figure 10a, b shows the specific volume profiles at different temperatures. One can see that these profiles increase linearly from 100 K to the specific temperatures and then increase with sharper slopes at temperatures higher than these specific temperatures. The melting temperature was determined by the intersection of two linear lines from the initial (100–300 K) and final ranges (370–800 K), as plotted in Fig. 10. The predicted melting temperature of PMMA is about 460 K, which is

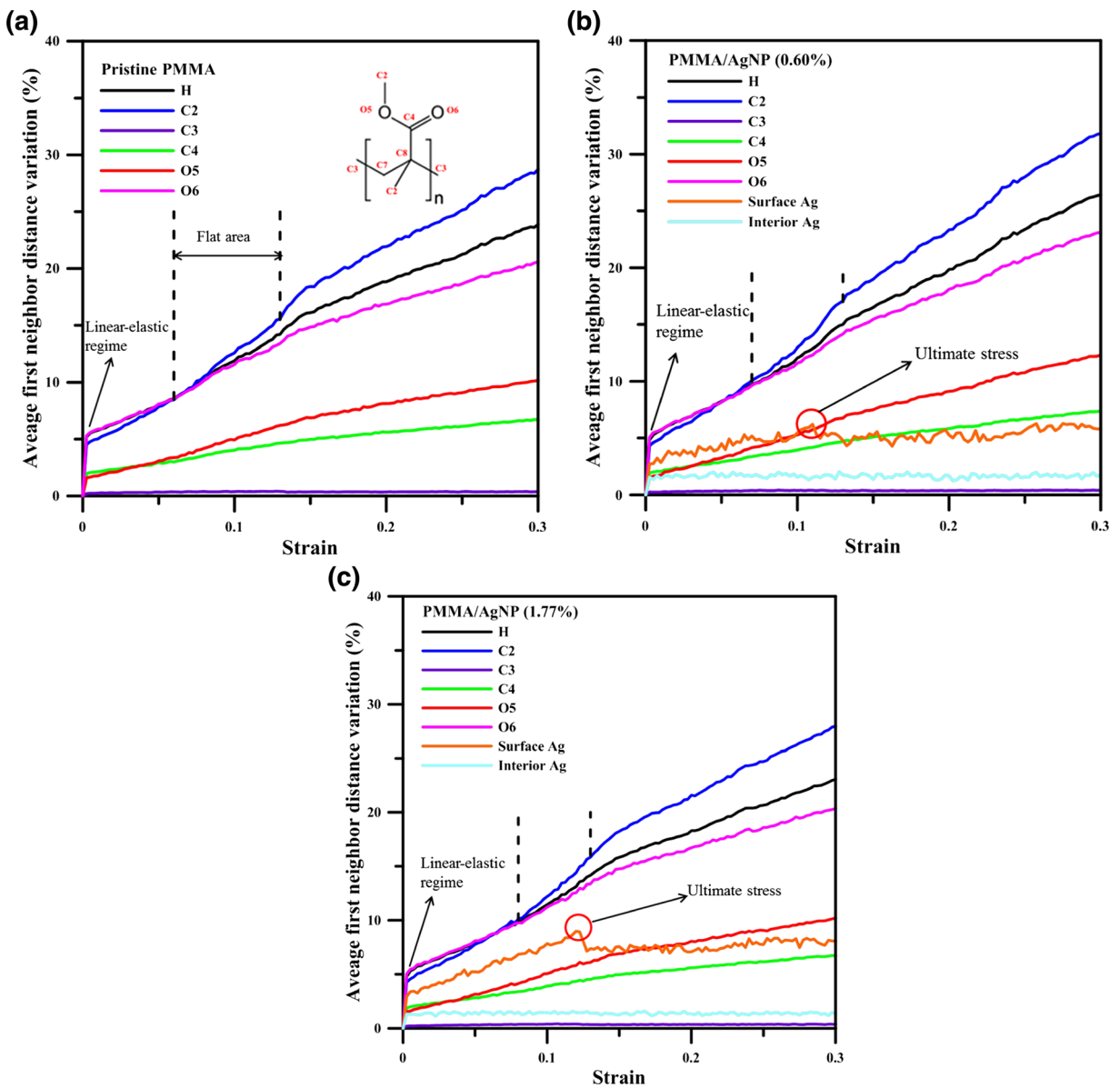


**Fig. 9** The profiles of average first neighbor distance variation of **a** pristine PMMA, **b** PMMA/AgNP (0.60%), and **c** PMMA/AgNP (1.77%) at different strains

close to the experimental value between 408 and 433 K (Nishi and Wang 1975). Because the specific volume profiles at higher temperatures are not completely linear, this is an approximate way to get the system melting point. The melting temperatures obtained by this way were only used for setting the simulation temperatures at which the structures are different from those below the melting temperature.

For further understanding the temperature effect on the mechanical properties of pristine PMMA and the PMMA/AgNP composite, tensile simulations were carried out both at their melting points and at temperatures higher than these melting points. Figure 11a, b shows the stress–strain curves of the pristine PMMA and the PMMA/AgNP composite and 1.77 (three AgNPs) wt% under tensile loading at temperatures 300, 450, and

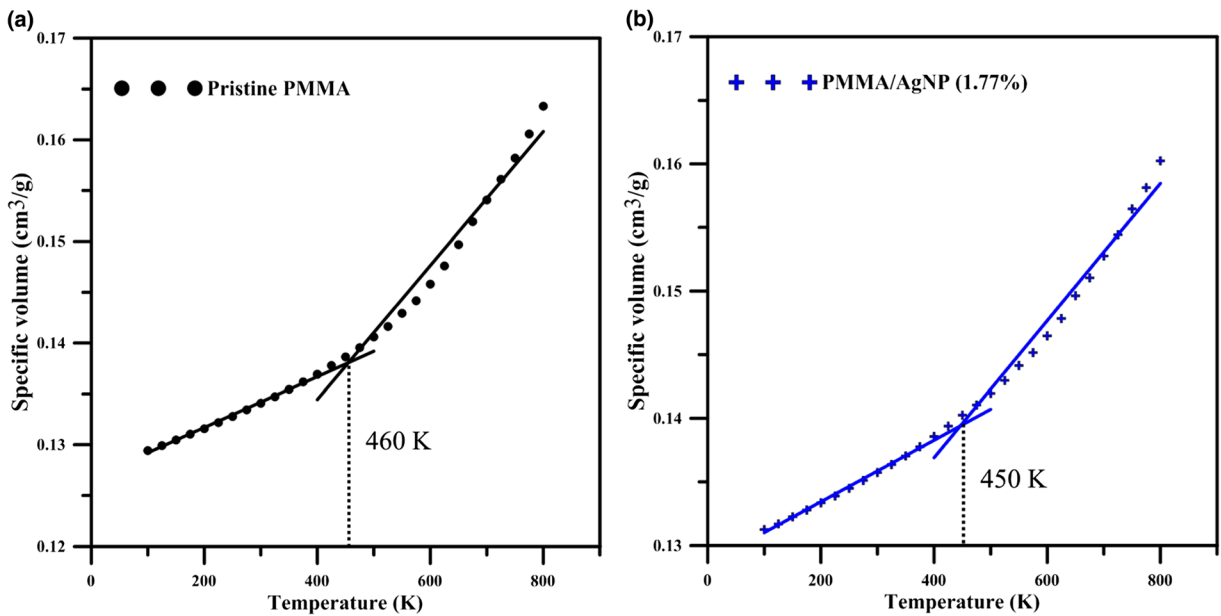


**Fig. 10** The specific volume at different temperatures during the temperature elevation process for **a** pristine PMMA and **b** PMMA/AgNP (1.77%)

550 K. It can be seen that ultimate tensile strength and Young’s modulus of PMMA at 300 K are higher than 450 and 550 K for both cases, indicating that the temperature has strong effect on the mechanical properties of both PMMA and PMMA/AgNP composites and the

mechanical properties undergo significant reduction at high temperatures. Details of mechanical properties of pristine PMMA and PMMA/AgNP (1.77%) derived from the stress–strain profiles of Fig. 11a, b are listed in Table 4. For pristine PMMA at temperatures of 300,

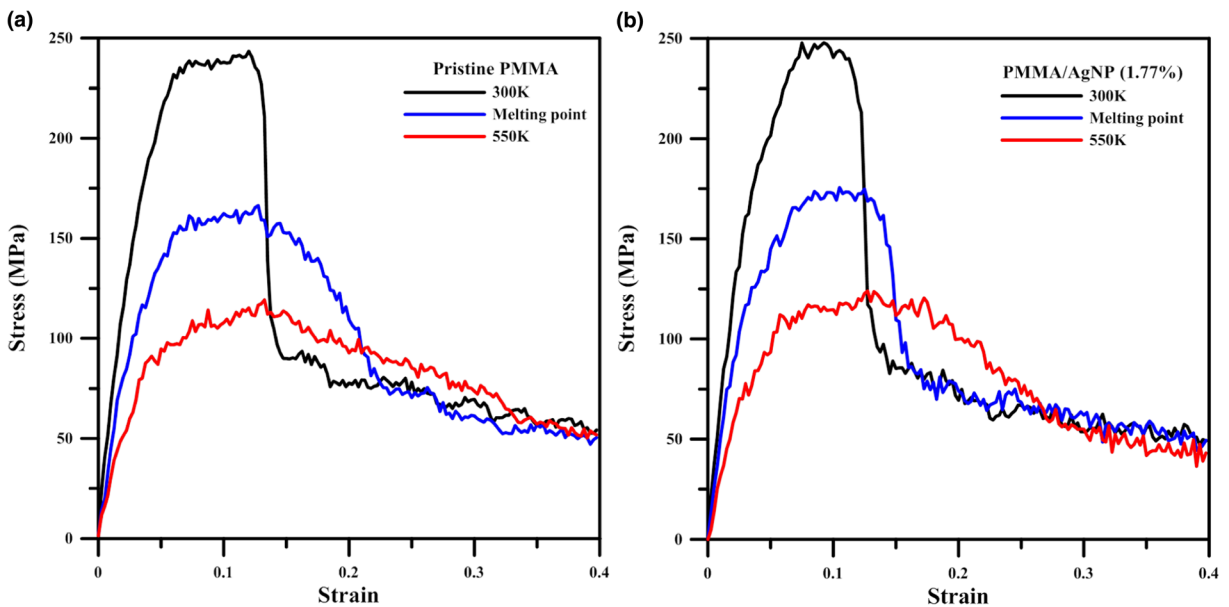


**Fig. 11** Stress–strain curves for **a** pristine PMMA and **b** PMMA/AgNP (1.77%) at 300, 450, and 550 K

**Table 5** The Young's modulus and ultimate stress of pristine PMMA and PMMA/AgNP (1.77%) at different temperatures

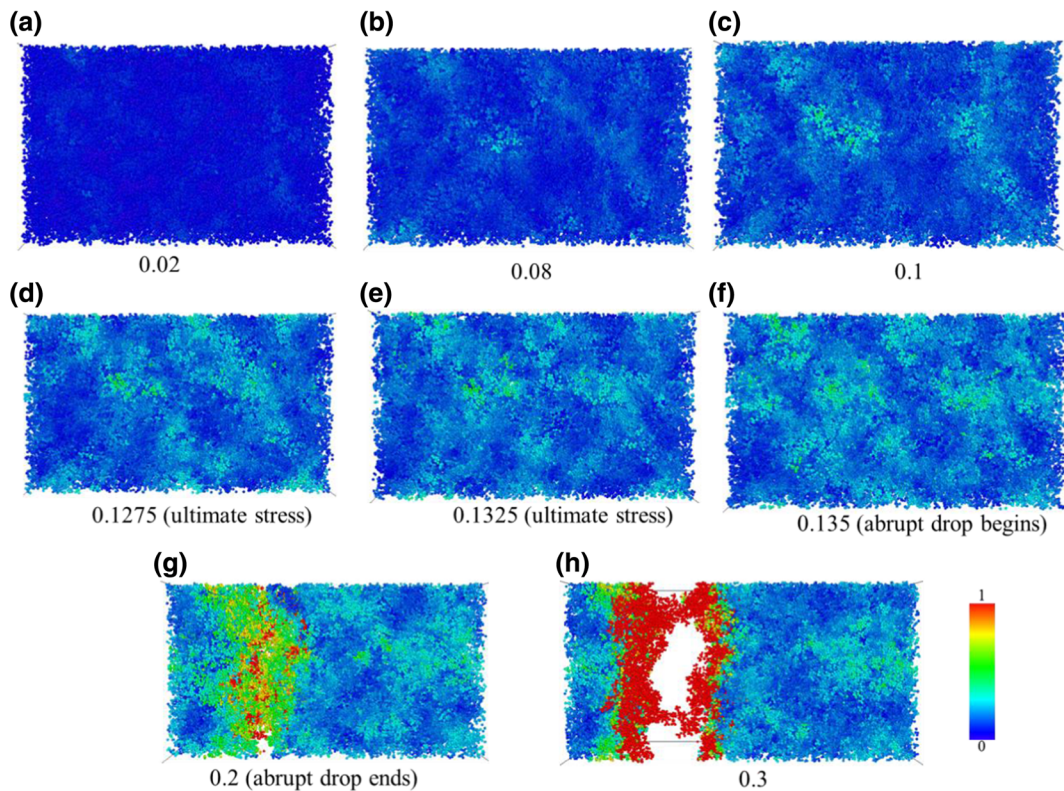
Temperature (K)	PMMA			PMMA/AgNP (1.77%)		
	300	450	550	300	450	550
Young's modulus (MPa)	5537.42	4772.34	4091.58	5842.94	5087.25	4201.23
Ultimate stress (MPa)	243.42	166.34	119.24	247.82	175.60	123.96

450, and 550 K, the Young's moduli are about 5537.42, 4772.34, and 4091.58 MPa, respectively. At 450 and 550 K, these reductions in Young's moduli are about 14 and 26% of pristine PMMA at 300 K. For ultimate stress or tensile strength at 450 and 550 K, it can also be seen in Table 4 that the tensile strength can be reduced from 243.42 to 166.34 and 119.24 MPa, decreased by about 32 and 51% of pristine PMMA at 300 K.

For PMMA/AgNP (1.77%) at 450 and 550 K, the Young's moduli are about 5087.25 and 4201.23 MPa, decrease about 13 and 28% of PMMA/AgNP (1.77%) at 300 K. Additionally, it can be seen that the ultimate tensile strength is reduced from 247.82 to 175.60 and

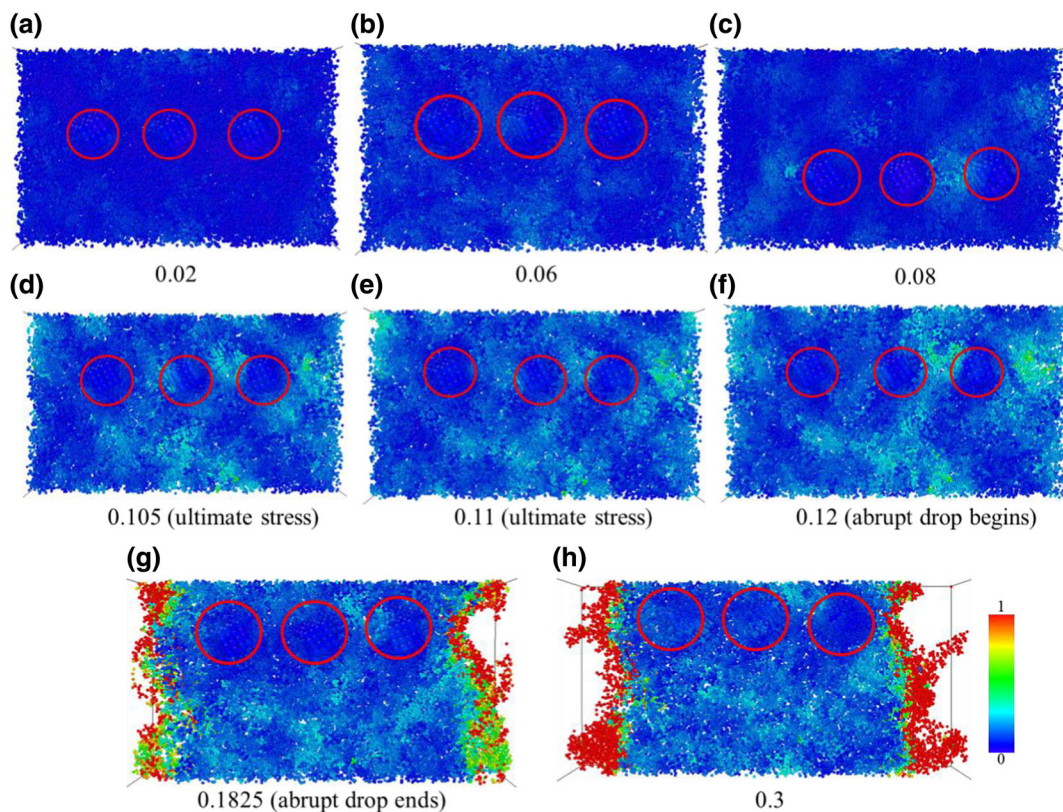
123.96 MPa at 450 and 550 K, a decrease of about 29 and 50% (Table 5).

Figure 12a–h shows the snapshots of pristine PMMA with atomic  $\eta_i^{\text{Mises}}$  values at strains of 0.02, 0.08, 0.1, 0.1275 (at ultimate stress), 0.1325 (ultimate stress), 0.135 (abrupt drop begins), 0.2 (abrupt drop ends), and 0.3 at 450 K. Compared with the snapshots at the corresponding strains for pristine PMMA at 300 K shown in Fig. 4a–h, Fig. 12h shows a void with a relatively smaller size than that shown in Fig. 4h, indicating that the pristine PMMA becomes more ductile when the temperature is close to its melting point. For PMMA/AgNP (1.77%) at 450 K, Fig. 13a–h indicates that the AgNPs possess



**Fig. 12** Uniaxial tensile deformation snapshots of pristine PMMA at **a** strain of 0.02, **b** 0.08, **c** 0.1, **d** 0.1275 (ultimate stress), **e** 0.1325 (ultimate stress), **f** 0.135 (abrupt drop begins), **g** 0.2

(abrupt drop ends), and **h** strain of 0.3 at 450 K. The atoms are colored by their corresponding local shear strain values according to the referenced structure at strain of 0



**Fig. 13** Uniaxial tensile deformation snapshots of PMMA/AgNP (1.77%) at **a** strain of 0.02, **b** 0.06, **c** 0.08, **d** 0.105 (ultimate stress), **e** 0.11 (ultimate stress), **f** 0.12 (abrupt drop begins), **g** 0.1825

(abrupt drop ends), and **h** strain of 0.3 at melting point 450 K. The atoms are colored by their corresponding local shear strain values according to the referenced structure at strain of 0

higher mobility within the PMMA matrix as compared with those in Fig. 6a–h. These AgNPs get closer when the strain increases, and the void appears within the region only having PMMA as shown in Fig. 13d.

## Conclusions

The mechanical behaviors of PMMA and PMMA/AgNP composites with different Ag weight fractions were investigated by the molecular dynamics tensile simulation. According to the RDF profiles at strain of 0, the AgNP surface shows stronger interaction strength and longer interaction distance with the PMMA chains than those between PMMA chains, resulting in the higher local PMMA density in the vicinity to the AgNP surface about 8.2 Å. At 300 K, the increases in Young's moduli of PMMA/AgNP (0.60%) and PMMA/AgNP (1.77%) are insignificant, and the tensile strength can

slightly be enhanced from 242.43 MPa for pristine to 247.82 MPa for PMMA/AgNP (1.77%), respectively.

The  $\eta_1^{\text{Mises}}$  evolution at different strains shows that the  $\eta_1^{\text{Mises}}$  values of PMMA atoms in the vicinity to the AgNP surface are relatively significant during the tensile process, indicating that the PMMA atoms in this region are under considerable shear deformation because of the interface formed by two materials with so different mechanical properties. By the analysis of average first neighbor distance, the variation of Ag atoms on the AgNP surface is more significant at the elastic region. After the strain increases to 0.02, the damaged areas appear on the methyl group of PMMA, but the backbone of PMMA is less affected during the tensile process.

For the temperature effect on the mechanical properties of pristine PMMA and PMMA/AgNP (1.77%), the tensile simulations were conducted at 450 and 550 K, which are close to the predicted melting point about 460 K of pristine PMMA by the temperature elevation process from 100 to 800 K. The simulation results show

that the PMMA materials at 450 and 550 K become more ductile than that at 300 K, because the void begins to appear at higher tensile strain. The Young's modulus and ultimate strength of PMMA decrease considerable with the increasing temperature. For PMMA/AgNP (1.77%) at 450 and 550 K, the AgNPs within the PMMA matrix show the higher mobility than those at 300 K and the AgNPs get closer as the strain increases. Accordingly, the fracture appears at the PMMA part of PMMA/AgNP (1.77%), resulting in the close Young's moduli and ultimate strengths of pristine PMMA and PMMA/AgNP (1.77%) at 450 and 550 K.

**Acknowledgements** The authors would like to thank the (1) Ministry of Science and Technology of Taiwan, under Grant No. MOST104-2221-E-110-008; (2) NSYSU-KMU Joint Research project (#NSYSUKMU 105-P024) from Kaohsiung Medical University for their support on this study; and (3) Prof. Jin-Yuan Hsieh of Minghsin University of Science and Technology and Mr. Chen-Yun Lin for their help on the revision of this study.

#### Compliance with ethical standards

**Conflict of interest** Shin-Pon Ju has received research grants from the Ministry of Science and Technology of Taiwan. Hsing-Yin Chen has received research grants from the NSYSU-KMU Joint Research project. Che-Wei Shih declares that he has no conflict of interest.

#### References

- Adnan A, Sun C, Mahfuz H (2007) A molecular dynamics simulation study to investigate the effect of filler size on elastic properties of polymer nanocomposites. *Compos Sci Technol* 67(3):348–356. <https://doi.org/10.1016/j.compscitech.2006.09.015>
- Agag T, Koga T, Takeichi T (2001) Studies on thermal and mechanical properties of polyimide–clay nanocomposites. *Polymer* 42(8):3399–3408. [https://doi.org/10.1016/S0032-3861\(00\)00824-7](https://doi.org/10.1016/S0032-3861(00)00824-7)
- Ahmad I, Unwin M, Cao H, Chen H, Zhao H, Kennedy A, Zhu Y (2010) Multi-walled carbon nanotubes reinforced Al<sub>2</sub>O<sub>3</sub> nanocomposites: mechanical properties and interfacial investigations. *Compos Sci Technol* 70(8):1199–1206. <https://doi.org/10.1016/j.compscitech.2010.03.007>
- Banks-Sills L, Shiber DG, Fourman V, Eliasi R, Shlayer A (2016) Experimental determination of mechanical properties of PMMA reinforced with functionalized CNTs. *Compos Part B* 95:335–345. <https://doi.org/10.1016/j.compositesb.2016.04.015>
- Blivli A, Benhui F, Bai J, Kondo D, Bédoui F (2016) Experimental evidence of size effect in nano-reinforced polymers: case of silica reinforced PMMA. *Polym Test* 56:337–343. <https://doi.org/10.1016/j.polymertesting.2016.10.025>
- Cheng S, Grest GS (2013) Molecular dynamics simulations of evaporation-induced nanoparticle assembly. *J Chem Phys* 138(6):064701. <https://doi.org/10.1063/1.4789807>
- Coleman JN, Khan U, Blau WJ, Gun'ko YK (2006) Small but strong: a review of the mechanical properties of carbon nanotube–polymer composites. *Carbon* 44(9):1624–1652. <https://doi.org/10.1016/j.carbon.2006.02.038>
- Fan J, Shi Z, Zhang L, Wang J, Yin J (2012) Aramid nanofiber-functionalized graphene nanosheets for polymer reinforcement. *Nano* 4(22):7046–7055
- Gilman JW (1999) Flammability and thermal stability studies of polymer layered-silicate (clay) nanocomposites. *Appl Clay Sci* 15(1):31–49. [https://doi.org/10.1016/S0169-1317\(99\)00019-8](https://doi.org/10.1016/S0169-1317(99)00019-8)
- Guo Z, Pereira T, Choi O, Wang Y, Hahn HT (2006) Surface functionalized alumina nanoparticle filled polymeric nanocomposites with enhanced mechanical properties. *J Mater Chem* 16(27):2800–2808. <https://doi.org/10.1039/b603020c>
- Hamed-Rad F, Ghaffari T, Rezaii F, Ramazani A (2014) Effect of nanosilver on thermal and mechanical properties of acrylic base complete dentures. *J dentistry (Tehran, Iran)* 11(5):495
- Heijboer J (1967) Dynamic mechanical properties and impact strength. *J Polymer Sci Part C: Polymer Symposia* 16(7):3755–3763. <https://doi.org/10.1002/polc.5070160716>
- Heinz H, Vaia R, Farmer B, Naik R (2008) Accurate simulation of surfaces and interfaces of face-centered cubic metals using 12-6 and 9-6 Lennard-Jones potentials. *J Phys Chem C* 112(44):17281–17290. <https://doi.org/10.1021/jp801931d>
- Hoover WG (1985) Canonical dynamics: equilibrium phase-space distributions. *Phys Rev A* 31(3):1695–1697. <https://doi.org/10.1103/PhysRevA.31.1695>
- Jia Z, Wang Z, Xu C, Liang J, Wei B, Wu D, Zhu S (1999) Study on poly (methyl methacrylate)/carbon nanotube composites. *Mater Sci Eng A* 271(1):395–400. [https://doi.org/10.1016/S0921-5093\(99\)00263-4](https://doi.org/10.1016/S0921-5093(99)00263-4)
- Ju S-P, Huang W-C, Lin K-H, Chen H-L, Lin J-S, Hsieh J-Y (2014) Mechanical properties of PGA at different water fractions—a molecular dynamics study. *RSC Adv* 4(25):12710–12715. <https://doi.org/10.1039/C4RA00484A>
- Karolewski MA (2001) Tight-binding potentials for sputtering simulations with fcc and bcc metals. *Radiation Effects Defects Solids* 153(3):239–255. <https://doi.org/10.1080/10420150108211842>
- Kendall MJ, Siviour CR (2014) Rate dependence of poly(vinyl chloride), the effects of plasticizer and time–temperature superposition. *Proceedings Royal Society A: Mathematical, Physical Engineering Sci* 470(2167):20140012. <https://doi.org/10.1098/rspa.2014.0012>
- Kim JS, Kuk E, Yu KN, Kim J-H, Park SJ, Lee HJ, Kim SH, Park YK, Park YH, Hwang C-Y (2007) Antimicrobial effects of silver nanoparticles. *Nanomedicine* 3(1):95–101. <https://doi.org/10.1016/j.nano.2006.12.001>
- Lee G-W, Park M, Kim J, Lee JI, Yoon HG (2006) Enhanced thermal conductivity of polymer composites filled with hybrid filler. *Compos A: Appl Sci Manuf* 37(5):727–734. <https://doi.org/10.1016/j.compositesa.2005.07.006>
- Lee H, Yeo SY, Jeong SH (2003) Antibacterial effect of nanosized silver colloidal solution on textile fabrics. *J Mater Sci* 38(10):2199–2204. <https://doi.org/10.1023/A:1023736416361>



- Leszczyńska A, Njuguna J, Pielichowski K, Banerjee J (2007) Polymer/montmorillonite nanocomposites with improved thermal properties: part I. Factors influencing thermal stability and mechanisms of thermal stability improvement. *Thermochim Acta* 453(2):75–96. <https://doi.org/10.1016/j.tca.2006.11.002>
- Lu HH, El-Amin SF, Scott KD, Laurencin CT (2003) Three-dimensional, bioactive, biodegradable, polymer–bioactive glass composite scaffolds with improved mechanical properties support collagen synthesis and mineralization of human osteoblast-like cells in vitro. *J Biomed Mater Res A* 64(3): 465–474. <https://doi.org/10.1002/jbm.a.10399>
- Morsy, M. A. and M. A. Al-Daous (2013). Mechanical properties evaluation of new AuNP-PMMA composite. *International Review of Chemical Engineering (IRECHE)*; Vol 5, No 1 (2013)
- Mulfinger L, Solomon SD, Bahadory M, Jeyarajasingam AV, Rutkowsky SA, Boritz C (2007) Synthesis and study of silver nanoparticles. *J Chem Educ* 84(2):322. <https://doi.org/10.1021/ed084p322>
- Nayebi P, Zaminpayma E (2016) A molecular dynamic simulation study of mechanical properties of graphene–polythiophene composite with Reax force field. *Phys Lett A* 380(4):628–633. <https://doi.org/10.1016/j.physleta.2015.11.026>
- Nishi T, Wang T (1975) Melting point depression and kinetic effects of cooling on crystallization in poly (vinylidene fluoride)-poly (methyl methacrylate) mixtures. *Macromolecules* 8(6):909–915. <https://doi.org/10.1021/ma60048a040>
- Park JH, Jana SC (2003) The relationship between nano- and micro-structures and mechanical properties in PMMA–epoxy–nanoclay composites. *Polymer* 44(7):2091–2100. [https://doi.org/10.1016/S0032-3861\(03\)00075-2](https://doi.org/10.1016/S0032-3861(03)00075-2)
- Petersson L, Kvien I, Oksman K (2007) Structure and thermal properties of poly (lactic acid)/cellulose whiskers nanocomposite materials. *Compos Sci Technol* 67(11):2535–2544. <https://doi.org/10.1016/j.compscitech.2006.12.012>
- Quang Huy T, Van Quy N, Anh-Tuan L (2013) Silver nanoparticles: synthesis, properties, toxicology, applications and perspectives. *Adv Nat Sci Nanosci Nanotechnol* 4(3):033001
- Rafiee MA, Rafiee J, Wang Z, Song H, Yu Z-Z, Koratkar N (2009) Enhanced mechanical properties of nanocomposites at low graphene content. *ACS Nano* 3(12):3884–3890. <https://doi.org/10.1021/nn9010472>
- Shimizu F, Ogata S, Li J (2007) Theory of shear banding in metallic glasses and molecular dynamics calculations. *Mater Trans* 48(11):2923–2927. <https://doi.org/10.2320/matertrans.MJ200769>
- Skakalova V, Dettlaff-Weglikowska U, Roth S (2005) Electrical and mechanical properties of nanocomposites of single wall carbon nanotubes with PMMA. *Synth Met* 152(1–3):349–352. <https://doi.org/10.1016/j.synthmet.2005.07.291>
- Sodagar A, Kassae MZ, Akhavan A, Javadi N, Arab S, Kharazifard MJ (2012) Effect of silver nano particles on flexural strength of acrylic resins. *J Prosthodontic Res* 56(2):120–124. <https://doi.org/10.1016/j.jpor.2011.06.002>
- Srolovitz D, Maeda K, Vitek V, Egami T (1981) Structural defects in amorphous solids statistical analysis of a computer model. *Philosophical Magazine A* 44(4):847–866. <https://doi.org/10.1080/01418618108239553>
- Stepanov A, Popok V, Khaibullin I, Kreibig U (2002) Optical properties of polymethylmethacrylate with implanted silver nanoparticles. *Nucl Instrum Methods Phys Res, Sect B* 191(1):473–477. [https://doi.org/10.1016/S0168-583X\(02\)00595-5](https://doi.org/10.1016/S0168-583X(02)00595-5)
- Stukowski A (2009) Visualization and analysis of atomistic simulation data with OVITO—the open visualization tool. *Model Simul Mater Sci Eng* 18(1):015012
- Stukowski A (2014) Computational analysis methods in atomistic modeling of crystals. *JOM* 66(3):399–407. <https://doi.org/10.1007/s11837-013-0827-5>
- Sun H (1994) Force field for computation of conformational energies, structures, and vibrational frequencies of aromatic polyesters. *J Comput Chem* 15(7):752–768. <https://doi.org/10.1002/jcc.540150708>
- van Oss CJ, Good RJ (1989) Surface tension and the solubility of polymers and biopolymers: the role of polar and apolar interfacial free energies. *J Macromolecular Science—Chemistry* 26(8):1183–1203
- Wang D, Zhu J, Yao Q, Wilkie CA (2002) A comparison of various methods for the preparation of polystyrene and poly (methyl methacrylate) clay nanocomposites. *Chem Mater* 14(9):3837–3843. <https://doi.org/10.1021/cm011656+>
- Wang J, Hodgson PD, Zhang J, Yan W, Yang C (2010) Effects of pores on shear bands in metallic glasses: a molecular dynamics study. *Comput Mater Sci* 50(1):211–217. <https://doi.org/10.1016/j.commatsci.2010.08.001>
- Yang S, Yu S, Cho M (2013) Influence of Thrower–Stone–Wales defects on the interfacial properties of carbon nanotube/polypropylene composites by a molecular dynamics approach. *Carbon* 55:133–143. <https://doi.org/10.1016/j.carbon.2012.12.019>
- Zeng J, Saltysiak B, Johnson W, Schiraldi DA, Kumar S (2004) Processing and properties of poly (methyl methacrylate)/carbon nano fiber composites. *Compos Part B* 35(2):173–178. [https://doi.org/10.1016/S1359-8368\(03\)00051-9](https://doi.org/10.1016/S1359-8368(03)00051-9)
- Zhao L, Song PA, Cao Z, Fang Z, Guo Z (2012) Thermal stability and rheological behaviors of high-density polyethylene/fullerene nanocomposites. *J Nanomater* 2012:5
- Zheng W, Wong S-C (2003) Electrical conductivity and dielectric properties of PMMA/expanded graphite composites. *Compos Sci Technol* 63(2):225–235. [https://doi.org/10.1016/S0266-3538\(02\)00201-4](https://doi.org/10.1016/S0266-3538(02)00201-4)
- Zhi C, Bando Y, Tang C, Kuwahara H, Golberg D (2009) Large-scale fabrication of boron nitride nanosheets and their utilization in polymeric composites with improved thermal and mechanical properties. *Adv Mater* 21(28):2889–2893. <https://doi.org/10.1002/adma.200900323>
- Zhou T, Zha J-W, Cui R-Y, Fan B-H, Yuan J-K, Dang Z-M (2011) Improving dielectric properties of BaTiO<sub>3</sub>/ferroelectric polymer composites by employing surface hydroxylated BaTiO<sub>3</sub> nanoparticles. *ACS Appl Mater Interfaces* 3(7):2184–2188. <https://doi.org/10.1021/am200492q>
- Zhu R, Pan E, Roy A (2007) Molecular dynamics study of the stress–strain behavior of carbon-nanotube reinforced Epon 862 composites. *Mater Sci Eng A* 447(1):51–57. <https://doi.org/10.1016/j.msea.2006.10.054>